

Self-organization of various "phase-separated" nanostructures in a single chemical vapor deposition

Jinmei Wang^{1,7,§}, Dongyue Xie^{2,§}, Zhen Li^{1,†} (云), Xiaohang Zhang³, Xing Sun⁴, Amanda L. Coughlin¹, Thomas Ruch¹, Qiang Chen⁵, Yaroslav Losovyj⁶, Seunghun Lee³, Heshan Yu³, Haidong Zhou⁵, Haiyan Wang⁴, Jian Wang², and Shixiong Zhang^{1,8} (云)

- ¹ Department of Physics, Indiana University, Bloomington, Indiana 47405, USA
- ² Department of Mechanical & Materials Engineering, University of Nebraska-Lincoln, Lincoln, Nebraska 68588, USA
- ³ Department of Materials Science and Engineering, University of Maryland, College Park, Maryland 20742, USA
- ⁴ School of Materials Engineering, Purdue University, West Lafayette, Indiana 47907, USA
- ⁵ Department of Physics and Astronomy, University of Tennessee, Knoxville, Tennessee 37996, USA
- ⁶ Department of Chemistry, Indiana University, Bloomington, Indiana 47408, USA
- ⁷ College of Optoelectronic Engineering, Chongqing University of Posts and Telecommunications, Chongqing 400065, China
- ⁸ Department of Materials Science and NanoEngineering, Rice University, Houston, Texas 77005, USA
- § Jinmei Wang and Dongyue Xie contributed equally to this work.

 $\ensuremath{\mathbb{G}}$ Tsinghua University Press and Springer-Verlag GmbH Germany, part of Springer Nature 2020

Received: 6 February 2020 / Revised: 27 March 2020 / Accepted: 7 April 2020

ABSTRACT

Chemical vapor deposition (CVD) is one of the most versatile techniques for the controlled synthesis of functional nanomaterials. When multiple precursors are induced, the CVD process often gives rise to the growth of doped or alloy compounds. In this work, we demonstrate the self-assembly of a variety of 'phase-separated' functional nanostructures from a single CVD in the presence of various precursors. In specific, with silicon substrate and powder of Mn and SnTe as precursors, we achieved self-organized nanostructures including Si/SiO_x core-shell nanowire heterostructures both with and without embedded manganese silicide particles, $Mn_{11}Si_{19}$ nanowires, and SnTe nanoplates. The Si/SiO_x core-shell nanowires embedded with manganese silicide particles were grown along the <111> direction of the crystalline Si via an Au-catalyzed vapor-liquid-solid process, in which the Si and Si and Si and Si material. No Si or Si/SiO_x core-shell nanowires and <100>-oriented Si/SiO_x core-shell nanowires, a promising thermoelectric material. No Si or Si/SiO_x core-shell nanowires and <100>-oriented Si/SiO_x promising thermoelectric material. No Si or Si/SiO_x core-shell nanowires down to the experimental limit. Topological crystalline insulator Si/SiO_x core-shell nanoplates with dominant Si/SiO_x core-shell nanoplates. While multiple-channel transport was observed in the Si/SiO_x nanoplates, it may not be related to the topological surface states due to surface oxidation. Finally, we carried out thermodynamic analysis and density functional theory calculations to understand the 'phase-separation' phenomenon and further discuss general approaches to grow phase-pure samples when the precursors contain residual impurities.

KEYWORDS

nanomaterials synthesis, silicon nanowires, topological crystalline insulators, phase separation, chemical vapor deposition

1 Introduction

Nanostructured solid-state materials often possess enhanced functional properties over their bulk counterparts and are the foundation of nanoscience and nanotechnology [1]. The most prominent example is the one-dimensional (1D) silicon nanowires which are promising building blocks for nanoscale devices including field effect transistors [2–4], solar cells [5, 6], lithium batteries [7], and thermoelectric devices [8, 9]. Adding metal nanoparticles or quantum dots into 1D silicon-based nanowires adds substantially more functionalities to the system, through for example surface plasmonic effects or quantum confinement, and hence offers great potential for optoelectronic and sensing applications [10–15]. Intermetallic silicide com-

pounds (e.g., manganese silicides) are another important family of silicon-based materials with a broad spectrum of intriguing physical (e.g., spintronic and thermoelectric) properties that can also be enhanced via nanostructuring [16–19]. Another remarkable material system in which nanostructuring enhances properties is the so-called topological (crystalline) insulators such as Bi₂Te₃ and SnTe [20–26] which have insulating bulk but metallic surface states. As an example, the metallic surface states in SnTe are topologically protected by crystalline symmetries [20] and can be manipulated by elastic strain engineering, offering great potential for tunable electronic applications. Nanostructures are highly desired for magnifying topological surface conduction because of their large surface-area-to-volume ratio and high flexibility under mechanical

[†]Present address: Quantum Optoelectronics Research Team, RIKEN Center for Advanced Photonics, Saitama 351-0198, Japan

stress [27-39].

One of the most effective techniques to synthesize these functional nanomaterials is the chemical vapor deposition (CVD) which often involves either a vapor-liquid-solid (VLS) process, a direct vapor-solid (VS) deposition, or both. For example, Au-catalyzed VLS with a gaseous precursor (e.g., silane) has been widely used to grow Si nanowires of high crystalline quality [40-46]. Topological crystalline insulator (TCI) nanowires and nanoplates were also successfully grown using their corresponding powder as precursors via a VLS process that is often accompanied with direct VS deposition [27, 35-38]. With multiple precursors in a single CVD reactor, doped or alloyed nanomaterials can be grown in a controlled fashion [47]. This controllable chemical doping or alloying is one of the most important approaches to tune and tailor material properties. In this work, we demonstrate, on the other hand, the selfassembly of various 'phase-separated' nanostructures in the presence of multiple precursors in a single CVD system. Using silicon substrates and powder of Mn and SnTe as precursors, we achieved a variety of self-organized nanostructures including different types of Si/SiO_x core-shell nanowire heterostructures, higher manganese silicide (Mn11Si19) nanowires, SnTe nanoplates, as well as Mn-containing nanowires and nanoparticles. The first type of Si/SiOx nanowires have embedded manganese silicide particles and were grown along the <111> direction via an Au-catalyzed VLS process. In contrast, direct VS deposition gave rise to the growth of a second type of Si/SiO_x nanowires along the <110> direction without embedded particles, as well as <100>-oriented manganese silicide nanowires; none of which contains Sn or Te impurities down to the experimental limit. On the other hand, the TCI SnTe nanoplates with dominant {100} and {111} facets were grown free of Mn (or Si) impurities despite the deposition of Mn-containing particles and nanowires in their vicinity. The self-organization of phase-separated nanostructures in the presence of multiple precursors highlights the possibility of and provides a general guidance of achieving phase-pure growth even if the precursors contain considerable amount of unavoidable impurities.

Experimental

2.1 Synthesis

The growth of various nanostructures was carried out via a vapor transport approach inside a three-zone tube furnace. A schematic of the experimental setup is shown in Fig. 1(a). Three zones are centered at -8" (zone 1), 0" (zone 2), and 8" (zone 3) respectively. Mn powder (Alfa Aesar, purity 99.95%) was placed in an alumina crucible upstream at -8" (zone 1 center), and SnTe powder (Alfa Aesar, purity 99.999%) in an alumina crucible was located at 0" (zone 2 center) downstream. The growth substrates were cut from wafers (with or without dry thermal oxide) and were coated with Au nanoparticles (Ted Pella, diameter 50 nm). Two substrates were placed in the region between the two crucibles, and three were located downstream from the SnTe powder (from ~ 5" to ~ 14"); in some occasions, two more substrates were placed under the crucible with SnTe at 0" and from \sim 2" to \sim 5" respectively. The growth temperatures of the three zones (zones 1, 2, and 3) were set to 1,050, 550, and 425 °C respectively. Zone 2 and zone 3 started ramping after zone 1 reached 1,050 °C and its temperature became relatively stable. The temperature profile measured independently is plotted in Fig. S1 in the Electronic Supplementary Material (ESM). Argon was used as the carrier gas at a flow rate of 20 sccm and the pressure was maintained at 30 Torr during the six-hour growth.

2.2 Characterization

The morphology and chemical composition of the nanostructures were characterized by a scanning electron microscopy (SEM) instrument (FEI Quanta 600F) equipped with an energy-dispersive X-ray spectroscopy (EDX) detector. Raman measurement was performed using a confocal Raman microscope system (Renishaw inVia) with a 532 nm laser at room temperature [48]. The Raman spectra were calibrated using the silicon peak at 520.5 cm⁻¹. The spectrum of each point in the map was taken with a 50× objective lens. Transmission electron microscopy (TEM) characterization was performed in a FEI Tecnai Osiris TEM equipped with a Super-X windowless EDX detector and operated at 200 kV. X-ray photoelectron spectroscopy (XPS) studies were performed using a PHI VersaProbe II instrument which was equipped with a focused monochromatic Al K α source. All XPS spectra were calibrated using the carbon 1s peak at 284.8 eV [48-50].

2.3 Device fabrication and electrical measurements

The nanoplate devices were directly fabricated on the growth substrate with a dry thermal oxide layer. The alignment markers and electrodes were patterned by standard electron-beam lithography using SEM (FEI Quanta 600F with NPGS) [51]. After the exposed e-beam resist was developed in methyl isobutyl ketone (MIBK)/isopropyl alcohol (IPA), Ti and Au for the electrodes were subsequently deposited on the device

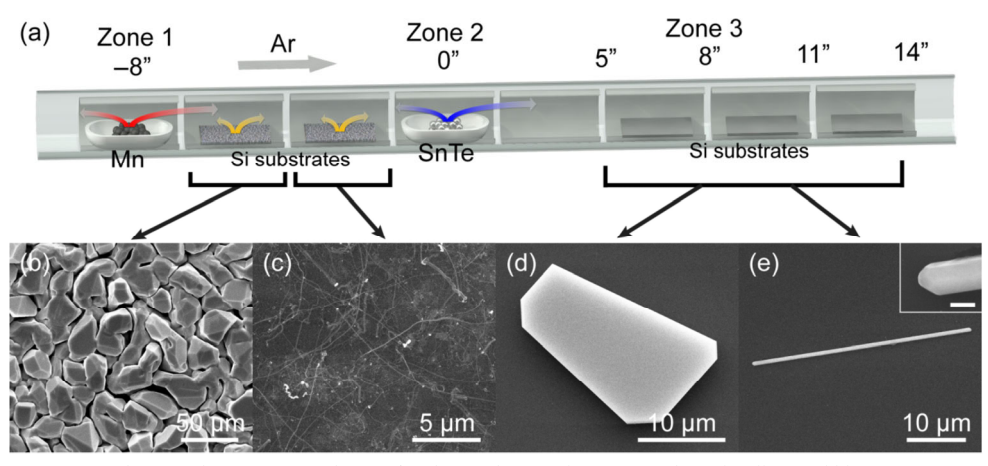


Figure 1 (a) Schematic picture showing the experimental setup for chemical vapor deposition. The red, yellow and blue arrows represent the diffusion of the vapor from Mn, Si substrates and SnTe, respectively. (b)-(e) SEM images taken from the representative nanostructures at different substrate locations in a single growth. The scale bar in the inset of (e) is 500 nm.

substrate by thermal evaporation (Boc Edwards Auto 306). The excessive metal was removed by a metal lift-off process in acetone. After connecting the gold pads of each plate in a Hall-bar configuration using a wire bonder, the sample was loaded into a physical property measurement system (PPMS, Quantum Design) for electronic transport measurements. A DC current of 10 mA was applied through the current leads of the sample and the polarity of the current was reversed for each measurement point to reduce the measurement error. The temperature dependence of the resistance was measured from 300 to 2 K with a cooling rate of 2 K/min. Magnetoresistance and Hall effect measurements were then carried out at selected temperatures. During the measurements, the scan rate of the magnetic field was kept at 0.2 T/min in the entire measurement range from -9 to 9 T. The symmetric component and the asymmetric component of the field-scan results were subsequently extracted to obtain the magnetoresistance and the Hall effect for each given temperature, respectively. The dimensions of the devices were characterized by atomic force microscopy (AFM) (Digital Instruments DimensionTM 5000).

2.4 Density functional theory calculations

Density functional theory (DFT) calculations were performed with Vienna *Ab initio* Simulation Package (VASP). Projector augmented wave (PAW) method, generalized gradient approximation (GGA), and Perdew-Burke-Ernzerhof (PBE) functional were used in this calculation. For Sn and Mn, s and d semi-core states are treated as valence states, respectively. The cut-off on kinetic energy for the plane waves basis set was set to 400 eV. For the calculation of the SnTe unit cell, a 12×12×12 MP k-points grid was used. For other calculations, the same k-point density was maintained. The self-consistent computation and geometry optimization were stopped with criteria of an energy change smaller than 10⁻⁶ eV and the force on atoms smaller than 0.001 eV/Å, respectively. The optimized lattice constant is 6.4075 Å, and the total energy of a Sn-Te pair was –7.5657 eV, consistent with previous studies [27].

3 Results and discussions

A variety of phase-separated nanostructures including manganese, silicon/silicon oxide, manganese silicide, and tin telluride were realized in a single CVD, in which the Mn powder, silicon substrates, and SnTe powder all served as precursors. In the three-zone tube furnace-based CVD setup (Fig. 1(a)), Mn and SnTe were placed in the center of zone 1 (-8") and zone 2 (0"), respectively, and the silicon substrates (either with or without a dry thermal oxide layer) were placed between them and downstream. SEM images of some typical nanostructures obtained from a representative growth are shown in Figs. 1(b)-1(e). Between zone 1 and 2, Mn-based microcrystals are densely distributed on the first substrate located from ~ -6" to -4" (Fig. 1(b), Figs. S2(a) and S3 in the ESM). The microcrystals were shown to contain Mn, and no Sn or Te impurities were detected by EDX or the more sensitive XPS from these microcrystals (Figs. S2(a) and S7 in the ESM). High density of nanowires with different morphologies were grown on the second substrate located from ~ -4 " to -1" (Fig. 1(c), and Fig. S4 in the ESM). These nanowires are rather thin, making detailed compositional characterization on each of them using SEM-based EDX challenging (Fig. S2(b) in the ESM). Nevertheless, XPS on a large area of such nanowires revealed that they contain a strong signal of Si along with weak Mn peak, but free of Sn or Te (Fig. S8 in the ESM). Furthermore, as will be demonstrated later by TEM studies, these nanowires are Si/SiO_x core-shell heterostructures and manganese silicide compound. On the substrates placed from $\sim 5"$ to $\sim 14"$ near zone 3, we obtained SnTe nanoplates (Fig. S5 in the ESM) as well as a relatively lower density of straight nanowires (Fig. S6 in the ESM). A typical nanoplate is shown in the SEM image of Fig. 1(d). The nanoplate has a well-defined shape with a lateral dimension of tens μm . EDX shows strong signals of Sn and Te from the nanoplate, while Mn peaks are not detected (Fig. S2(c) in the ESM). Figure 1(e) shows a straight nanowire with a length of $\sim 38~\mu m$ and a diameter of $\sim 587~nm$. In contrast to the nanoplates, the straight nanowires contain Mn, but not Sn or Te (Fig. S2(d) in the ESM).

Because of their abundance in our growth and their functional properties in general, our focus in the following discussion will be on the Si-based nanowires and SnTe-based nanoplates. In particular, more systematic compositional and structural characterizations were carried out at the atomic scale to demonstrate their phase separation and to understand their growth mechanisms. We focus first on the three types of Si-based nanowires observed on the growth substrate located between ~ -4 " and ~ -1 ". The type-1 nanowires are Si/SiO_x core-shell heterostructures, which appear to be curvy with a diameter of tens nm. Catalyst particles were observed at the tip of these nanowires. TEM-EDX taken from a representative nanowire suggests that the nanowire body is composed of Si and O, while the catalyst particle at the tip of the nanowire contains mainly Au and Mn, as shown in Fig. 2(a) and Fig. S9 in the ESM. Although EDX mapping (Fig. 2(a)) seems to indicate an oxygen signal in the catalyst particle, the corresponding spectrum (Fig. S9(b) in the ESM) shows a broad background instead of a characteristic peak at the oxygen edge; therefore, the concentration of oxygen (if any) is negligible in the catalyst particle. Neither Sn nor Te is detected in the nanowires or in the nanoparticles. The Si/SiO_x nanowires may be grown via diffusion of atoms from the silicon substrate or through a VLS process which requires the creation of Si vapor. The latter mechanism is supported by the observation of pits on the Si substrates (Fig. S10 in the ESM) and the existence of a nanoparticle at the nanowire tip. In other words, these nanowires were grown using Au as the catalyst and Si as both the precursor and the substrate. The growth process is hence different from the conventional Au-catalyst VLS which often involves the decomposition of hash chemical gases (e.g., SiH₄ or SiCl₄) [45] and the oxide-assisted growth, in which silicon oxide, instead of Au, promotes the nucleation and growth [52].

We further carried out a control experiment without SnTe in zone 2 to understand its influence on the Si/SiO_x nanowire growth. As shown in Fig. S11 in the ESM, nanowires with similar morphology were grown from the substrate, indicating a negligible influence of SnTe on the growth of Si nanowires although tellurium may facilitate the sublimation of silicon [53]. EDX mapping at the nanowire body shows that the wire is Si-rich in the core and O-rich towards the surface (Fig. 2(b)), confirming a Si/SiO_x core-shell heterostructure. A closer look of the mapping in Fig. 2(a) indicates the existence of a Mn-rich nanoparticle in the Si/SiO_x nanowire near the alloy particle. This can be seen more clearly in Fig. 3(a), in which the Mn-rich particle is in the body of the Si/SiO_x core-shell nanowire. Since the silicon signal does not diminish in the particle region, it is reasonable to believe that the particle is manganese silicide alloy. High-resolution TEM (HRTEM) images in Figs. 3(b) and 3(c) suggest that the Si core is crystalline whereas the SiO_x shell is amorphous. The fast Fourier transform (FFT) taken in the Si core region (inset of Fig. 3(c)) indicates that the nanowire was grown along the <111> direction, which is the dominant

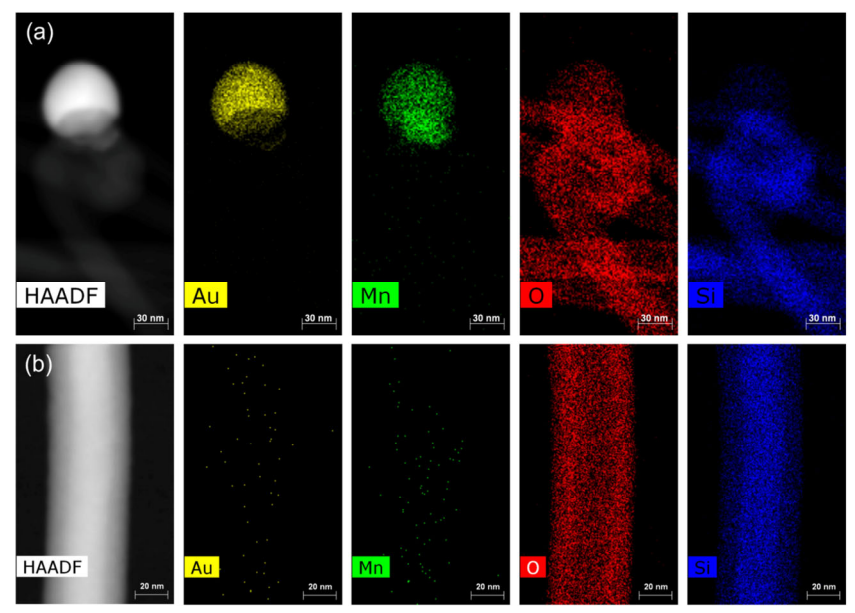


Figure 2 High-angle annular dark-field (HAADF) images and EDX mapping of individual elements taken from (a) the tip of a representative type-1 nanowire, as well as (b) the body of another representative type-1 nanowire. The oxygen signal in the core region is collected from the front and back of the nanowire in the direction of electron beam.

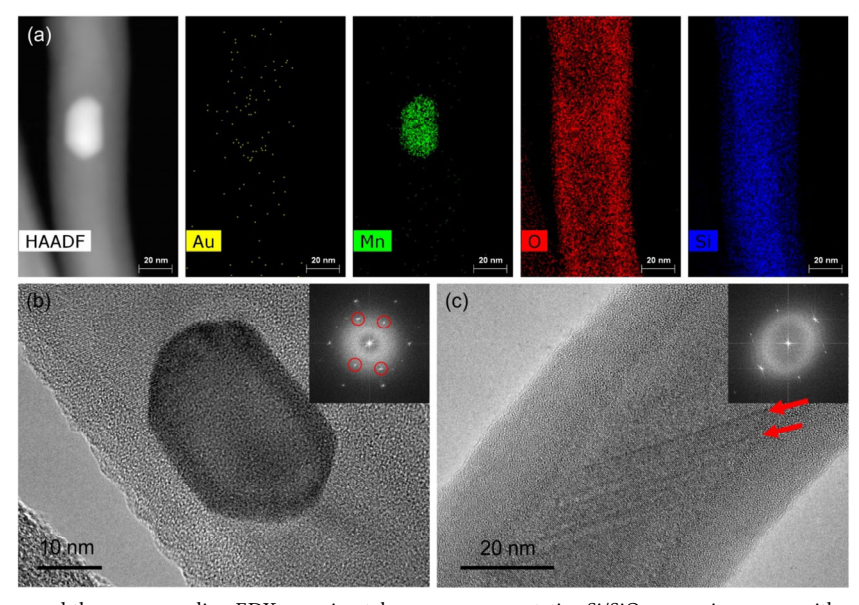


Figure 3 (a) HAADF image and the corresponding EDX mapping taken on a representative Si/SiOx nanowire grown without using the SnTe precursor. (b) HRTEM image of the same Si/SiOx nanowire with an embedded nanoparticle. The inset shows an FFT pattern that contains spots from Si (red circles) and from the particle (the rest). (c) HRTEM image of another representative Si/SiO_x nanowire in a region without the embedded nanoparticle. The red arrows denote stacking faults on the $[1\overline{1}1]$ plane.

growth direction for Au-catalyst of Si nanowires [54]. Stacking faults were observed on the [111] plane, as evidenced by the parallel lines with dark contrast in the HRTEM image and the corresponding stripes in the FFT pattern (Fig. 3(c) and its inset). The FFT taken in the particle region contains two sets of patterns: one from Si and the other from manganese silicide alloy (inset of Fig. 3(b)). To verify if the manganese silicide nanoparticles are embedded in the nanowires, TEM studies were performed with the sample being tilted along x and yaxes. Four images were taken with the tilting angle of the two axes oriented at either -30° or 30°. As seen clearly in Fig. S12 in the ESM, from all the viewing directions, the bright particles are always observed inside the nanowire, which suggests that they are indeed embedded in the nanowire. Figure S13 in the ESM shows the EDX mapping of these particles and four additional nanowires with particles embedded in their bodies

to justify the statistical significance.

The second type of nanowires are also Si/SiO_x core-shell heterostructures but with a distinct morphology. As shown in Fig. 4(a), and Fig. S14 in the ESM, the nanowires' cores are long, straight, and surrounded by a shell with sawtooth-like edges. The EDX mapping in Fig. 4(c) reveals that the core of the nanowire is dominated by Si, while the shell of the nanowire is composed of Si and O, with no Mn, Sn or Te signal detected in the body of the nanowire. Therefore, the chemical identity of type-2 nanowires is similar to that of type-1, with a Si core and silicon oxide shell, although no manganese silicide alloy particle is observed in this case. In contrast to the type-1 nanowires, the Si core in the type-2 is found to be grown along its <110> axis (Fig. 4(b)). The absence of Au nanoparticle at the nanowire tip indicates a direct VS growth rather than the Au-catalyzed VLS. The oxide shell is much thicker than a typical

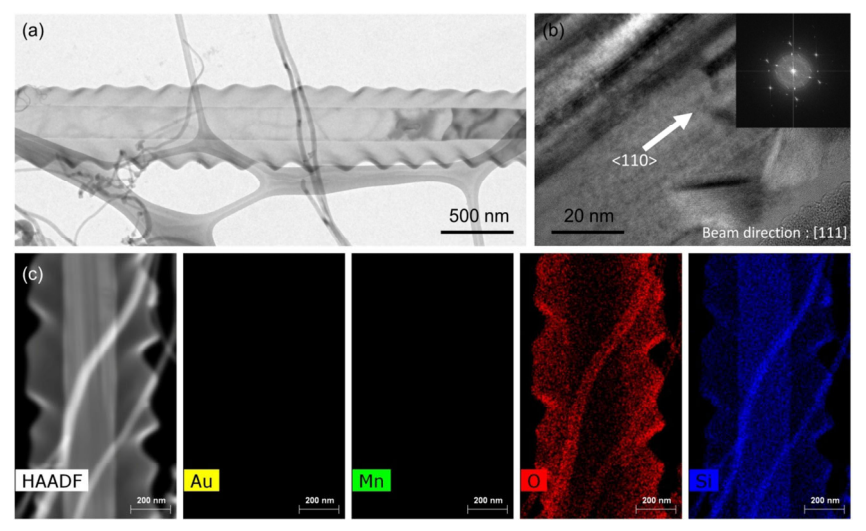


Figure 4 (a) Low magnification TEM image, (b) HRTEM image and FFT, (c) HAADF image and EDX mapping of individual elements taken from representative type-2 nanowires.

native silicon oxide layer, hence it is unlikely to be formed due to post-oxidation after growth. Instead, the well-defined sawtooth-like edges imply that the oxide shell is formed at an elevated temperature. Therefore, the growth may be attributed to an oxide-assisted process [55-57] in which the background oxygen in the CVD system plays an important role. In brief, a crystalline SiO nanowire is first formed via a direct VS process in the presence of silicon vapor and oxygen from the background followed by a separation of crystalline Si core and amorphous SiO2 shell as a result of the chemical reaction SiO + $SiO = Si + SiO_2$ [55–57]. As previously demonstrated, one of the dominant growth directions of the nanowires grown by the oxide-assisted process is <110> [52], consistent with our observation here. The existence of a thick oxide layer in the Au-catalyzed, type-1 nanowires also indicates the presence of a considerable amount of residual oxygen in the growth process.

Beyond Si/SiO_x core-shell heterostructures, we have also achieved nanowires of higher manganese silicide (Mn₁₁Si₁₉) which is a promising thermoelectric material [17]. Figure 5 shows the TEM images of a representative nanowire which is smooth and straight with a length of $\sim 1~\mu m$ and a diameter of $\sim 79~nm$. No Au particles are observed on either end of the nanowire, again indicating a direct VS growth. The nanowire body is single crystalline as evidenced by the clear atomic fringes in the HRTEM image (Fig. 5(b)) and the diffraction spots in the FFT (Fig. 5(c)). The EDX mapping in Fig. 5(d)

reveals that the nanowire is composed of uniformly distributed Si and Mn elements, and the outer region of the nanowire has a thin layer dominated by oxygen. Based on the FFT and EDX mapping, we conclude that this type of nanowire is single-crystalline $Mn_{11}Si_{19}$ grown along [100] direction and covered by a thin layer of oxide on its surface. The oxide layer in the $Mn_{11}Si_{19}$ nanowire is much thinner than that of the type-1 and -2 nanowires and is likely due to post-oxidation at an ambient environment. This indicates that the manganese silicide alloy compound is less prone to oxygen than the Si. More TEM images of type-3 nanowires are presented in Fig. S15 in the ESM.

One may think that the absence of Sn or Te (down to the experimental limit) in the three types of Si-based nanowires is simply because the nanowires were upstream in the carrier gas flow where the Sn or Te vapor could not reach; however as shown in Fig. S16 in the ESM, vapors from the downstream SnTe powder can easily diffuse upstream in a typical CVD. The absence of Sn and Te in the three types of nanowires may be attributed to two related reasons: 1) in the entire growth process, the upstream substrates, where the Si-based nanowires grow, are at a higher temperature than the solid SnTe precursor downstream; 2) Sn and Te have vapor pressures that are orders of magnitude higher than that of Si at the same temperature (e.g., $P_{\rm Sn}$: $\sim 3 \times 10^{-5}$ Torr and $P_{\rm Te2}$: $4-5 \times 10^2$ Torr versus $P_{\rm Si}$: $1-2 \times 10^{-8}$ Torr at ~ 925 °C) [58]. As a result, the vapor to solid reaction rate for Si on the upstream substrates is significantly

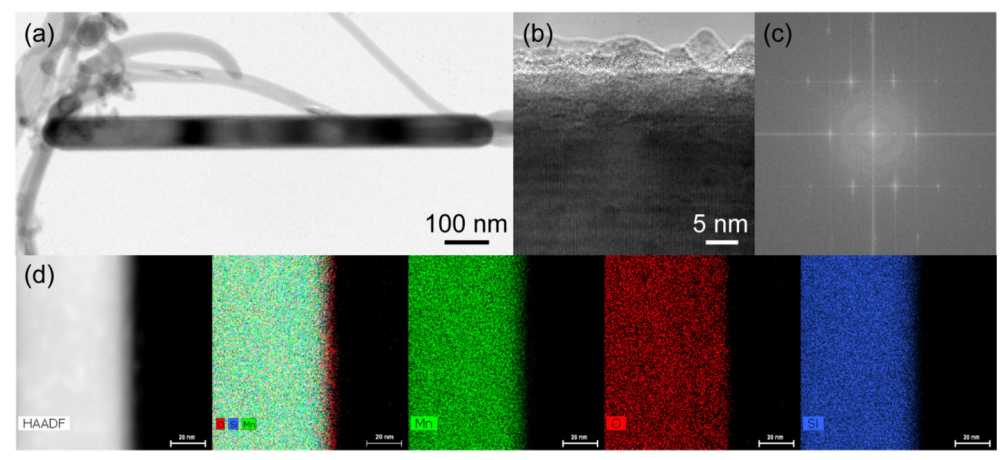


Figure 5 (a) TEM image of a representative type-3 nanowire. (b) HRTEM image and (c) FFT taken from a part of the nanowire body. (d) HAADF image and EDX mapping of individual elements taken from the nanowire body.

higher than that for Sn and Te, which can result in low Sn and Te concentration down below the detection limit in the nanowires grown via a VS process. The absence of Sn and Te in the type-1 nanowires and the corresponding Au catalyst particles also suggests a much lower absorption rate of these two species in the Au liquid droplet, in comparison to the Si.

Another interesting feature of the type-1 Si/SiO_x core-shell nanowires is the formation of manganese silicide alloy particles in the crystalline Si cores. According to the Mn-Si binary phase diagram, Mn is insoluble in solid Si; instead they can form a variety of manganese silicide compounds. The partial pressure of Si vapor is believed to be higher than that of Mn at the location of the nanowire growth, as the Si substrate itself acts as a precursor that supplies the Si vapor. As a result, Si reaches supersaturation in the Au liquid particle and precipitates into the solid phase more rapidly than Mn. When Mn supersaturates in the liquid particle and precipitates into the existing solid Si, it forms a manganese silicide phase which is separated from the pure Si phase, as suggested by the Mn-Si phase diagram. In other words, manganese silicide must present in the form of nanoparticles (or clusters) in the Si nanowires, as observed. The detection of Mn in the Au particle at room temperature (Fig. 2(a)) is qualitatively consistent with the relatively high solubility of Mn in solid Au (~15% according to the phase diagram). Our approach can be easily applied to the VLS growth of other particle-nanowire hybrid systems that may have great potential for optoelectronic and sensing applications [10-14], as long as the metal precursor is soluble in the catalyst but not in the nanowire.

We now turn to the discussion of topological crystalline insulator SnTe nanoplates grown on the substrates downstream. As shown in Figs. 6(a)-6(c), the nanoplates grown on the same substrate have various morphologies and orientations with respect to the substrate. In Fig. 6(a), the nanoplate is grown upon the substrate with a {100} facet of SnTe in parallel with the substrate. The side facets of this nanoplate consist of {100} and {111} planes of SnTe. In Fig. 6(b), two nanoplates are stacked together by the {100} facet upon the substrate. Their side facets are also {100} and {111} planes, and the orientation of the top nanoplate is rotated with respect to the one at the bottom. Nanoplates are also grown intercepting the substrate, as shown in Fig. 6(c), despite the same arrangement of crystal facets as the nanoplates grown upon the substrate. Similar morphology was observed in the undoped SnTe nanoplates that were grown in the absence of Mn and Si precursors. The observation of {100} and {111} facets is also consistent with the DFT calculation which shows that the two surfaces have relatively low surface energies [27, 59].

The large thickness of the nanoplates makes TEM characterizations of their crystal structures challenging. We therefore carried out Raman measurements to characterize the structural phase of the nanoplates. SnTe with a rock-salt crystal structure is expected in theory to have zero Raman active phonon modes, but experimentally, SnTe bulk crystals often show two Raman peaks at ~ 124 and ~ 142 cm⁻¹, which was previously attributed to crystal defects, the breaking of surface symmetry, and lately to the presence of Te due to surface oxidation [60–63]. These two characteristic Raman peaks are observed in our nanoplates (Fig. 6(d)). Raman mapping based on the area intensity of the two peaks (124 and 141 cm⁻¹) is presented in Fig. 6(e), showing good uniformity in the lateral dimension. Notably, particles containing Mn are observed in the vicinity of SnTe nanoplates (Figs. 6(f) and 6(g)), which suggests that Mn vapor can reach the growth region of SnTe in the CVD process. This argument is also supported by the observation of Mn-containing nanowires on the substrate downstream (Fig. 1(e)).

Nevertheless, no Mn (or Si) impurity was detected in the SnTe nanoplates down to the experimental limit. XPS survey obtained on a representative SnTe nanoplate (Fig. S17 in the ESM) only showed Sn, Te, and O peaks, and no Mn (or Si) peaks were present (binding energies are marked by vertical dashed lines). Figure 7 presents the high resolution of XPS spectra of a representative nanoplate with a large lateral size. Before sputtering, there are two peaks in the O 1s spectrum (Fig. 7(a)) where the dominant peak at ~ 532.6 eV corresponds to a -2oxidation state as in SiO₂, and the weaker peak at ~ 530.2 eV is likely contributed by the surface oxides of the nanoplate. In the Sn 3d spectrum before sputtering (Fig. 7(b)), the two components at 494.7 and 486.3 eV are assigned to a +4 oxidation state as in SnO₂, and the two components at 582.9 and 572.5 eV in the Te 3d spectrum (Fig. 7(c)) are attributed to elemental Te in a 0 oxidation state. These oxidation products have also been detected on the surface of SnTe single crystals and doped SnTe nanostructures [49, 63, 64]. No distinguishable peaks were found in the Mn 2p spectrum before sputtering. Since XPS is a surface-sensitive technique, we carried out Ar sputtering for 10 min to remove the surface oxides and probe the possible trace of Mn deeper in the pristine region of the same nanoplate.

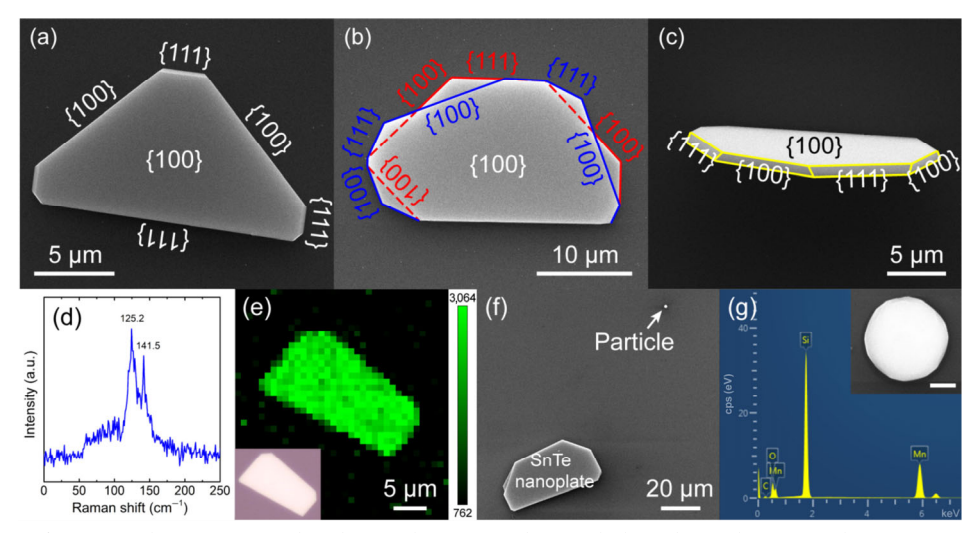


Figure 6 SEM images of (a) a nanoplate grown upon the substrate, (b) two nanoplates stacked together, and (c) a nanoplate grown intercepting the substrate. (d) Single acquisition Raman spectrum and (e) Raman mapping from a representative nanoplate. Inset is an optical image of the same nanoplate. (f) SEM image showing the presence of a particle near a SnTe nanoplate and (g) the EDX spectrum taken from the particle. The scale bar in the inset of (g) is 500 nm.

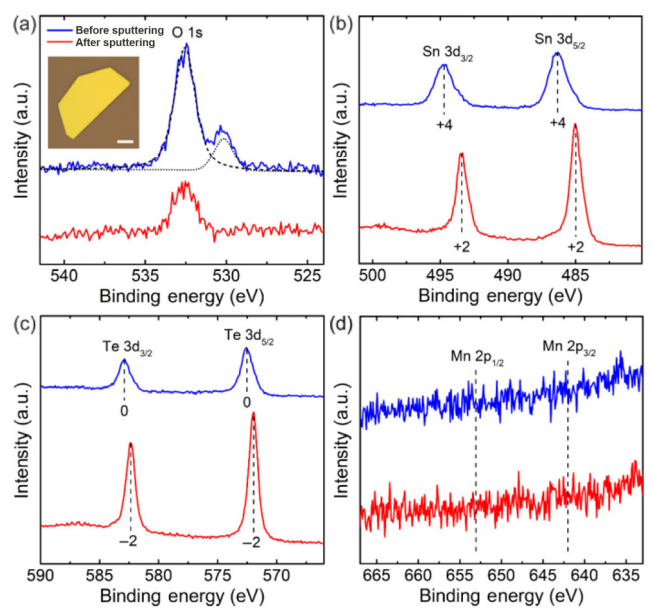


Figure 7 High resolution XPS core level spectra of (a) O 1s, (b) Sn 3d, (c) Te 3d, and (d) Mn 2p obtained from an individual nanoplate, before and after 10 min sputtering respectively. The spectra before sputtering were calibrated using the C 1s peak, and the spectra after sputtering were calibrated using the O 1s peak due to the absence of the C 1s peak. The scale bar in the inset of (a) is $20 \, \mu m$.

After sputtering, the oxygen peak corresponding to surface oxides of SnTe together with the Te⁰ and Sn⁴⁺ peaks disappeared, indicating the removal of surface oxides. Meanwhile, Sn in the +2 oxidation state with binding energies 493.4 and 485.0 eV, as well as Te in the −2 oxidation state with binding energies 582.4 and 571.9 eV appeared, thus the pristine SnTe was exposed. Again, there were no peaks in the Mn 2p spectrum within the detection limit of XPS. The possible locations of Mn²⁺ peaks are marked by dashed lines in Fig. 7(d) [65].

Furthermore, magneto-transport and Hall measurements were carried out on the SnTe nanoplates. The temperature dependence of longitudinal resistance R_{xx} (Fig. 8(a)) shows a metallic behavior, as observed previously in bulk and nanostructured SnTe without intentional doping [35, 66]. The metallic transport is attributed to the existence of high-density Sn vacancies which act as p-type dopants in SnTe [66, 67]. The dR_{xx}/dT increases rapidly below \sim 97 K (the inset of Fig. 8(a)), corresponding to a small kink in the R_{xx} -T curve at the same temperature range. A kink in the R_{xx} -T curve of SnTe signifies a ferroelectric phase transition from cubic to rhombohedral structure [68, 69]. The Hall resistivity (ρ_{xy}) at 300 K shows a linear dependence on the magnetic field B (Fig. 8(b)), from

which the hole concentration is determined to be 4.9×10^{20} cm⁻³ and the hole mobility to be ~ 95 cm²/(V·s). As the temperature decreases down to 200 K, the ρ_{xy} -B deviates from a linear relation at high magnetic fields, indicating the appearance of more than one conduction channel. The non-linear deviation becomes more prominent at lower temperatures (i.e., 2 and 20 K). The crystal mirror symmetry is partially broken when the structure is transitioning from cubic to rhombohedral; therefore, the more prominent non-linearity below the transition temperature indicates that the multiple-channel conduction is likely to be a pure bulk effect rather than from topological surface states. This may be due to the surface oxidation as seen in XPS studies as well as the large thickness of the nanoplates.

Manganese doping can induce long-range magnetic order in SnTe [70], and the magnetic ground state is sensitive to the chemical potential (or charge carrier density) [71]. The ferromagnetism mediated by charge carriers gives rise to spin-splitting in the conduction band and the valence band. When the bottom conduction band and the top valence band cross each other, the system transits into a magnetic Weyl semimetal (WSM) state [72]. While a WSM phase has not been experimentally realized in SnTe, ferromagnetism and its related spin transport were reported in Mn-doped bulk samples [70, 73–75]. Notably, Mn doping of only 0.04, at. % can lead to a negative magnetoresistance in SnTe crystals. [75] Yet, positive magnetoresistance was observed in our nanoplates at all temperatures (Fig. 8(c)), suggesting that the concentration of Mn impurity, if any, should be less than 0.04%. The weak antilocalization effect detected in SnTe thin films [76] is not observed here in our nanoplates. In conventional metals with only one type of charge carrier, the magnetoresistance follows a quadratic dependence on the magnetic field B. As shown in the inset of Fig. 8(c), the magnetoresistance deviates from B^2 at about 3 T, which is consistent with the existence of multiple conduction channels.

Lastly, we discuss the underlying mechanism for the absence of Mn impurity down to the experimental limit. The solubility of Mn in SnTe is $\sim 3\%$ at a growth temperature of ~ 500 °C [77]. According to the Hall measurement, the percentage of Sn vacancies in the undoped SnTe nanoplates is as large as ~ 3 at. %. When Mn and SnTe with 3% Sn deficiency are present, one may expect to have Mn occupy the Sn vacancy site and form Mn-doped SnTe. To understand why this is not the case, we calculated the formation energy of a Sn vacancy and a Mn substitutional atom using DFT. The formation energy of neutral defects can be calculated as Eq. (1) [78, 79]

$$\Delta H[X] = E_{\text{tot}}[X] - E_{\text{tot}}[\text{bulk}] - \sum n_i \mu_i$$
 (1)

Where $E_{\text{tot}}[X]$ is the total energy of supercell containing a defect

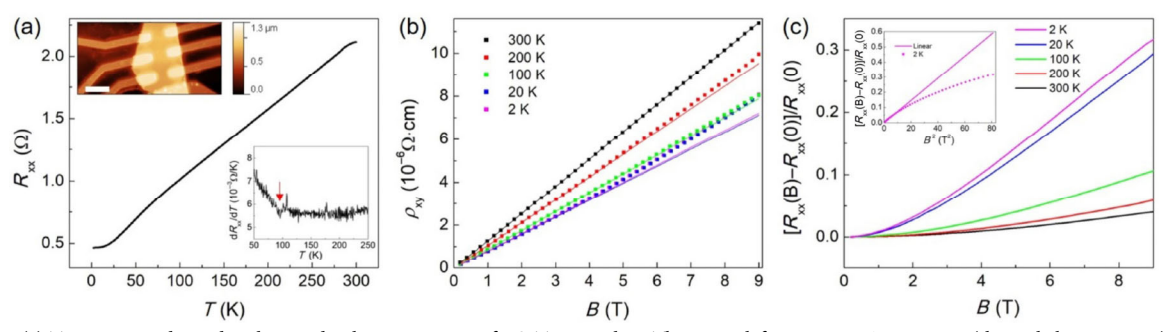


Figure 8 (a) Temperature-dependent longitudinal resistance R_{xx} of a SnTe nanoplate. The upper left inset is an AFM image (the scale bar is 10 μm), and the lower right inset is a plot of dR_{xx}/dT versus T. The red arrow in the lower right inset indicates the change of slope (or a kink) in the resistance plot. (b) Hall resistivity $ρ_{xy}$ as a function of the magnetic field B measured at different temperatures. The solid squares are experimental data and the solid lines are linear fitting at low field. (c) Magnetoresistence versus B at different temperatures. The inset shows magnetoresistence versus B^2 at 2 K to illustrate the deviation from the quadratic behavior.

X, $E_{tot}[bulk]$ is the total energy of supercell containing no defects, n_i is the number of i atoms added into the supercell (when removing atoms, $n_i < 0$), and μ_i is the chemical potential of i atom.

The chemical potential of elements depends on the environment. For Sn and Te, their chemical potential is related by Eq. (2)

$$\mu_{\rm Sn} + \mu_{\rm Te} = E_{\rm tot} [\rm SnTe] \tag{2}$$

The upper limit on μ_{Sn} is equal to the total energy of a Sn atom in the stable face-centered cubic phase

$$\mu_{\rm Sn}^{\rm max} = \mu_{\rm Sn[bulk]} \tag{3}$$

The lower limit on μ_{Sn} will be reached when μ_{Te} has maximum value

$$\mu_{\rm Sn}^{\rm min} = E_{\rm tot} [SnTe] - \mu_{\rm Te[bulk]} \tag{4}$$

The chemical potential of the impurity element Mn has a maximum value equal to the total energy of a Mn atom in the stable cubic phase. In this condition, the formation energy of the Mn substitutional atom in SnTe will have a minimum value. When $\mu_{\rm Mn}$ reaches the upper bound, the formation energy of a Mn substitutional atom at different environments is in the range of 2.20 to 2.77 eV. In comparison, the formation energy of a Sn vacancy varies from -0.08 to 0.5 eV. Therefore, the Sn vacancy has a lower formation energy than the Mn substitutional atom for all possible chemical potentials, which explains the absence of detectable Mn doping in the SnTe nanoplate.

The self-organization of phase-separated nanostructures observed in the presence of multiple precursors suggests that one can tailor the CVD growth condition to achieve pure products even if the precursors are not pure. This is particularly useful when the precursors unavoidably contain significant amount of residual impurities or the availability of pure precursors is limited by its remarkably high cost. Based on our growth results and analysis, we reveal three factors that play crucial roles in achieving phase-pure samples or in minimizing impurity concentration in an equilibrium condition: 1) the solubility of impurities in the product. Since the solubility of a solid solution is mainly determined by its temperature, the temperature of the growth substrate is an important parameter to tailor for achieving "phase-pure" growth. For VLS growth of nanowires, the solubility of impurity in the catalyst particles plays a crucial role; in principle, one could choose the catalyst in which the impurity is insoluble to achieve pure VLS-grown nanowires. 2) Vapor pressure difference. One should minimize both the sublimation of impurity in the precursor and the VS deposition of impurity in the product. As such, one should choose a precursor temperature at which the vapor pressure of the impurity is significantly lower than that of the main precursor and a substrate temperature at which the vapor pressure of the impurity is higher than that of the main product. The partial pressure can be tuned to be greatly lower than the vapor pressure of the impurity to minimize its vaporsolid reaction. 3) The stability of native defects; in particular, the vacancies. As shown in our Mn-SnTe growth and the corresponding DFT calculations, the relatively easy formation of vacancies can inhibit the substitutional doping. For binary products, a cation-poor condition often suppresses the doping of cation impurities, while an anion-poor condition in general limits anion impurities.

Conclusion

In summary, we demonstrated the self-organization of a variety of "phase-separated" nanostructured materials using multiple precursors in a single CVD process. The CVD growth involves silicon substrates and powder of Mn and SnTe as precursors, and the self-organized nanostructures include two different types of Si/SiOx core/shell nanowire heterostructures, higher manganese silicide nanowires, and SnTe nanoplates. The first type of Si/SiO_x nanowires were grown along the <111> direction via an Au-catalyzed VLS mechanism and were embedded with manganese silicide particles in the crystalline Si core. In contrast, direct VS deposition led to <110>-oriented Si/SiO_x nanowires free of embedded particles as well as <100>-oriented Mn11Si19 nanowires, a promising thermoelectric material. No Sn or Te impurities were detected in the nanowires down to the experimental limit. On the other hand, SnTe nanoplates with dominant {100} and {111} facets were found to be free of Mn (and Si) impurities despite the deposition of nanoparticles and nanowires containing Mn in their vicinity. The phase separation of those nanostructures is well understood based on thermodynamic analysis and DFT calculations. Our work highlights the possibility of simultaneously synthesizing distinct functional nanomaterials in a single CVD system without causing cross-contamination. It also suggests that one can tailor the CVD condition to achieve phase-pure samples even if the precursors contain a considerable amount of unavoidable impurities. Finally, it provides a useful approach to grow nanoparticle-nanowire hybrid systems via a VLS process.

Acknowledgements

We thank Prof. X. F. Qian for helpful discussions, W. Yang and M. Hosek for experimental assistance. We are also grateful to Y. Zhao and Prof. D. Li for some preliminary thermal transport characterization efforts which prompted the authors to conduct more thorough analyses of the synthesized nanostructures. This work was supported, in part, by the Indiana University Vice Provost for Research through the Faculty Research Support Program, National Science Foundation Research Experience for Undergraduates grant PHY-1757646, NSF-DMR-1350002. We thank the Indiana University-Bloomington Nanoscale Characterization Facility (NCF) for the use of instruments (The XPS instrument at NCF was funded through grant NSF-DMR-1126394).

Electronic Supplementary Material: Supplementary material (temperature profile of the tube furnace, EDX spectra taken from different microcrystals/nanostructures, low-magnification SEM images to show the distribution of different microcrystals /nanostructures, XPS spectra taken from Mn-related microcrystals and Si-based nanowires, HAADF image and EDX spectra taken from a nanowire body and its nanoparticle tip, SEM image showing Si pits on the substrate, optical micrograph and SEM image showing the nanowires grown without the use of SnTe precursor, HAADF images of the nanoparticles embedded in a Si-based nanowire taken along different directions, TEM characterizations of more type-1, type-2 and type-3 nanowires to demonstrate the statistical significance, photo showing the evidence of vapor diffusion, and XPS survey taken on a representative SnTe nanoplate) is available in the online version of this article at https://doi.org/10.1007/s12274-020-2798-5.

References

- [1] Lieber, C. M. Nanoscale science and technology: Building a big future from small things. MRS Bull. 2003, 28, 486-491.
- Huang, Y.; Duan, X. F.; Cui, Y.; Lauhon, L. J.; Kim, K. H.; Lieber, C. M. Logic gates and computation from assembled nanowire building blocks. Science 2001, 294, 1313-1317.



- [3] Cui, Y.; Zhong, Z. H.; Wang, D. L.; Wang, W. U.; Lieber, C. M. High performance silicon nanowire field effect transistors. *Nano Lett.* 2003, 3, 149–152.
- [4] Cui, Y.; Duan, X. F.; Hu, J. T.; Lieber, C. M. Doping and electrical transport in silicon nanowires. J. Phys. Chem. B 2000, 104, 5213–5216.
- [5] Tian, B. Z.; Zheng, X. L.; Kempa, T. J.; Fang, Y.; Yu, N. F.; Yu, G. H.; Huang, J. L.; Lieber, C. M. Coaxial silicon nanowires as solar cells and nanoelectronic power sources. *Nature* 2007, 449, 885–889.
- [6] Garnett, E.; Yang, P. D. Light trapping in silicon nanowire solar cells. *Nano Lett.* 2010, 10, 1082–1087.
- [7] Chan, C. K.; Peng, H. L.; Liu, G; McIlwrath, K.; Zhang, X. F.; Huggins, R. A.; Cui, Y. High-performance lithium battery anodes using silicon nanowires. *Nat. Nanotechnol.* **2008**, *3*, 31–35.
- [8] Boukai, A. I.; Bunimovich, Y.; Tahir-Kheli, J.; Yu, J. K.; Goddard III, W. A.; Heath, J. R. Silicon nanowires as efficient thermoelectric materials. In *Materials For Sustainable Energy: A Collection of Peer-Reviewed Research and Review Articles from Nature Publishing Group*. Dusastre, V., Ed.; Singapore: World Scientific, 2010; pp 116–119.
- [9] Hochbaum, A. I.; Chen, R. K.; Delgado, R. D.; Liang, W. J.; Garnett, E. C.; Najarian, M.; Majumdar, A.; Yang, P. D. Enhanced thermoelectric performance of rough silicon nanowires. *Nature* 2008, 451, 163–167
- [10] Kang, M.; Yuwen, Y.; Hu, W. C.; Yun, S.; Mahalingam, K.; Jiang, B.; Eyink, K.; Poutrina, E.; Richardson, K.; Mayer, T. S. Self-organized freestanding one-dimensional Au nanoparticle arrays. *ACS Nano*. 2017, 11, 5844–5852.
- [11] Park, G. S.; Kwon, H.; Lee, E. K.; Kim, S. K.; Lee, J. H.; Li, X. S.; Chung, J. G.; Heo, S.; Song, I. Y.; Lee, J. H. et al. Fabrication of surface plasmon-coupled Si nanodots in Au-embedded silicon oxide nanowires. Adv. Mater. 2010, 22, 2421–2425.
- [12] Pescaglini, A.; Iacopino, D. Metal nanoparticle–semiconductor nanowire hybrid nanostructures for plasmon-enhanced optoelectronics and sensing. J. Mater. Chem. C 2015, 3, 11785–11800.
- [13] Hu, M. S.; Chen, H. L.; Shen, C. H.; Hong, L. S.; Huang, B. R.; Chen, K. H.; Chen, L. C. Photosensitive gold-nanoparticle-embedded dielectric nanowires. *Nat. Mater.* 2006, 5, 102–106.
- [14] Lin, X.; Li, S. H.; Lu, K. Q.; Tang, Z. R.; Xu, Y. J. Constructing film composites of silicon nanowires@CdS quantum dot arrays with ameliorated photocatalytic performance. *New J. Chem.* 2018, 42, 14096–14103.
- [15] Agarwal, D.; Aspetti, C. O.; Cargnello, M.; Ren, M. L.; Yoo, J.; Murray, C. B.; Agarwal, R. Engineering localized surface plasmon interactions in gold by silicon nanowire for enhanced heating and photocatalysis. *Nano Lett.* 2017, 17, 1839–1845.
- [16] Higgins, J. M.; Schmitt, A. L.; Guzei, I. A.; Jin, S. Higher manganese silicide nanowires of nowotny chimney ladder phase. *J. Am. Chem.* Soc. 2008, 130, 16086–16094.
- [17] Girard, S. N.; Chen, X.; Meng, F.; Pokhrel, A.; Zhou, J. S.; Shi, L.; Jin, S. Thermoelectric properties of undoped high purity higher manganese silicides grown by chemical vapor transport. *Chem. Mater.* 2014, 26, 5097–5104.
- [18] Pokhrel, A.; Degregorio, Z. P.; Higgins, J. M.; Girard, S. N.; Jin, S. Vapor phase conversion synthesis of higher manganese silicide (MnSi_{1,75}) nanowire arrays for thermoelectric applications. *Chem. Mater.* 2013, 25, 632–638.
- [19] Higgins, J. M.; Ding, R. H.; DeGrave, J. P.; Jin, S. Signature of helimagnetic ordering in single-crystal MnSi nanowires. *Nano Lett.* 2010, 10, 1605–1610.
- [20] Fu, L. Topological crystalline insulators. Phys. Rev. Lett. 2011, 106, 106802
- [21] Hsieh, T. H.; Lin, H.; Liu, J. W.; Duan, W. H.; Bansil, A.; Fu, L. Topological crystalline insulators in the SnTe material class. *Nat. Commun.* 2012, 3, 982.
- [22] Tanaka, Y.; Ren, Z.; Sato, T.; Nakayama, K.; Souma, S.; Takahashi, T.; Segawa, K.; Ando, Y. Experimental realization of a topological crystalline insulator in SnTe. *Nat. Phys.* 2012, 8, 800–803.
- [23] Dziawa, P.; Kowalski, B. J.; Dybko, K.; Buczko, R.; Szczerbakow, A.; Szot, M.; Łusakowska, E.; Balasubramanian, T.; Wojek, B. M.; Berntsen, M. H. et al. Topological crystalline insulator states in Pb_{1-x}Sn_xSe. *Nat. Mater.* 2012, 11, 1023–1027.
- [24] Okada, Y.; Serbyn, M.; Lin, H.; Walkup, D.; Zhou, W. W.; Dhital, C.; Neupane, M.; Xu, S. Y.; Wang, Y. J.; Sankar, R. et al. Observation

- of Dirac Node Formation and Mass Acquisition in a topological crystalline insulator. *Science* **2013**, *341*, 1496–1499.
- [25] Xu, S. Y.; Liu, C.; Alidoust, N.; Neupane, M.; Qian, D.; Belopolski, I.; Denlinger, J. D.; Wang, Y. J.; Lin, H.; Wray, L. A. et al. Observation of a topological crystalline insulator phase and topological phase transition in Pb_{1-x}Sn_xTe. Nat. Commun. 2012, 3, 1192.
- [26] Littlewood, P. B.; Mihaila, B.; Schulze, R. K.; Safarik, D. J.; Gubernatis, J. E.; Bostwick, A.; Rotenberg, E.; Opeil, C. P.; Durakiewicz, T.; Smith, J. L. et al. Band structure of SnTe studied by photoemission spectroscopy. *Phys. Rev. Lett.* 2010, 105, 086404.
- [27] Li, Z.; Shao, S.; Li, N.; McCall, K.; Wang, J.; Zhang, S. X. Single crystalline nanostructures of topological crystalline insulator SnTe with distinct facets and morphologies. *Nano Lett.* 2013, 13, 5443–5448.
- [28] Wang, Q. S.; Cai, K. M.; Li, J.; Huang, Y.; Wang, Z. X.; Xu, K.; Wang, F.; Zhan, X. Y.; Wang, F. M.; Wang, K. Y. et al. Rational design of ultralarge Pb_{1-x}Sn_xTe nanoplates for exploring crystalline symmetry-protected topological transport. *Adv. Mater.* 2016, 28, 617–623.
- [29] Xu, E. Z.; Li, Z.; Acosta, J. A.; Li, N.; Swartzentruber, B.; Zheng, S. J.; Sinitsyn, N.; Htoon, H.; Wang, J.; Zhang, S. X. Enhanced thermoelectric properties of topological crystalline insulator PbSnTe nanowires grown by vapor transport. *Nano Res.* 2016, 9, 820–830.
- [30] Zou, Y. C.; Chen, Z. G.; Kong, F. T.; Lin, J.; Drennan, J.; Cho, K.; Wang, Z. C.; Zou, J. Planar vacancies in Sn_{1-x}Bi_xTe nanoribbons. ACS Nano. 2016, 10, 5507–5515.
- [31] Saghir, M.; Sanchez, A. M.; Hindmarsh, S. A.; York, S. J.; Balakrishnan, G. Nanomaterials of the topological crystalline insulators, Pb_{1-x}Sn_xTe and Pb_{1-x}Sn_xSe. Cryst. Growth Des. 2015, 15, 5202–5206.
- [32] Safdar, M.; Wang, Q. S.; Mirza, M.; Wang, Z. X.; Xu, K.; He, J. Topological surface transport properties of single-crystalline SnTe nanowire. *Nano Lett.* 2013, 13, 5344–5349.
- [33] Wei, F.; Liu, C. W.; Li, D.; Wang, C. Y.; Zhang, H. R.; Sun, J. R.; Gao, X. P. A.; Ma, S.; Zhang, Z. D. Broken mirror symmetry tuned topological transport in PbTe/SnTe heterostructures. *Phys. Rev. B* 2018, 98, 161301.
- [34] Liu, C. W.; Wei, F.; Premasiri, K.; Liu, S. H.; Ma, S.; Zhang, Z. D.; Gao, X. P. A. Non-Drude magneto-transport behavior in a topological crystalline insulator/band insulator heterostructure. *Nano Lett.* 2018, 18, 6538–6543.
- [35] Shen, J.; Jung, Y.; Disa, A. S.; Walker, F. J.; Ahn, C. H.; Cha, J. J. Synthesis of SnTe nanoplates with {100} and {111} surfaces. *Nano Lett.* 2014, 14, 4183–4188.
- [36] Saghir, M.; Lees, M. R.; York, S. J.; Balakrishnan, G. Synthesis and characterization of nanomaterials of the topological crystalline insulator SnTe. Cryst. Growth Des. 2014, 14, 2009–2013.
- [37] Safdar, M.; Wang, Q. S.; Mirza, M.; Wang, Z. X.; He, J. Crystal shape engineering of topological crystalline insulator SnTe microcrystals and nanowires with huge thermal activation energy gap. *Cryst. Growth Des.* 2014, 14, 2502–2509.
- [38] Zou, Y. C.; Chen, Z. G.; Lin, J.; Zhou, X. H.; Lu, W.; Drennan, J.; Zou, J. Morphological control of SnTe nanostructures by tuning catalyst composition. *Nano Res.* 2015, 8, 3011–3019.
- [39] Qian, X. F.; Fu, L.; Li, J. Topological crystalline insulator nanomembrane with strain-tunable band gap. *Nano Res.* 2015, 8, 967–979.
- [40] Wagner, R. S.; Ellis, W. C. Vapor-liquid-solid mechanism of single crystal growth. Appl. Phys. Lett. 1964, 4, 89–90.
- [41] Cui, Y.; Lauhon, L. J.; Gudiksen, M. S.; Wang, J. F.; Lieber, C. M. Diameter-controlled synthesis of single-crystal silicon nanowires. *Appl. Phys. Lett.* 2001, 78, 2214–2216.
- [42] Hochbaum, A. I.; Fan, R.; He, R. R.; Yang, P. D. Controlled growth of Si nanowire arrays for device integration. *Nano Lett.* 2005, 5, 457–460.
- [43] Westwater, J.; Gosain, D. P.; Tomiya, S.; Usui, S.; Ruda, H. Growth of silicon nanowires via gold/silane vapor-liquid-solid reaction. *J. Vac. Sci. Technol. B* 1997, 15, 554–557.
- [44] Allen, J. E.; Hemesath, E. R.; Perea, D. E.; Lensch-Falk, J. L.; Li, Z. Y.; Yin, F.; Gass, M. H.; Wang, P.; Bleloch, A. L.; Palmer, R. E. et al. High-resolution detection of Au catalyst atoms in Si nanowires. *Nat. Nanotechnol.* 2008, 3, 168–173.
- [45] Schmidt, V.; Wittemann, J. V.; Senz, S.; Gösele, U. Silicon nanowires: A review on aspects of their growth and their electrical properties. *Adv. Mater.* 2009, 21, 2681–2702.

- [46] Yang, C.; Zhong, Z. H.; Lieber, C. M. Encoding electronic properties by synthesis of axial modulation-doped silicon nanowires. Science **2005**, 310, 1304-1307.
- [47] Duan, X.; Lieber, C. M. General synthesis of compound semiconductor nanowires. Adv. Mater. 2000, 12, 298-302.
- [48] Li, Z.; Yang, W. C.; Losovyj, Y.; Chen, J.; Xu, E. Z.; Liu, H. M.; Werbianskyj, M.; Fertig, H. A.; Ye, X. C.; Zhang, S. X. Large-size niobium disulfide nanoflakes down to bilayers grown by sulfurization. Nano Res. 2018, 11, 5978-5988.
- [49] Li, Z.; Xu, E. Z.; Losovyj, Y.; Li, N.; Chen, A. P.; Swartzentruber, B.; Sinitsyn, N.; Yoo, J.; Jia, Q. X.; Zhang, S. X. Surface oxidation and thermoelectric properties of indium-doped tin telluride nanowires. Nanoscale 2017, 9, 13014-13024.
- [50] Yang, W. C.; Xie, Y. T.; Sun, X.; Zhang, X. H.; Park, K.; Xue, S. C.; Li, Y. L.; Tao, C. G.; Jia, Q. X.; Losovyj, Y. et al. Stoichiometry control and electronic and transport properties of pyrochlore Bi₂Ir₂O₇ thin films. Phys. Rev. Mater. 2018, 2, 114206.
- [51] Yang, W. C.; Coughlin, A. L.; Webster, L.; Ye, G. H.; Lopez, K.; Fertig, H. A.; He, R.; Yan, J. A.; Zhang, S. X. Highly tunable Raman scattering and transport in layered magnetic Cr₂S₃ nanoplates grown by sulfurization. 2D Mater. 2019. 6, 035029.
- [52] Zhang, R. Q.; Lifshitz, Y.; Lee, S. T. Oxide-assisted growth of semiconducting nanowires. Adv. Mater. 2003, 15, 635-640.
- [53] Fardy, M.; Hochbaum, A. I.; Goldberger, J.; Zhang, M. M.; Yang, P. Synthesis and thermoelectrical characterization of lead chalcogenide nanowires. Adv. Mater. 2007, 19, 3047-3051.
- [54] Morales, A. M.; Lieber, C. M. A laser ablation method for the synthesis of crystalline semiconductor nanowires. Science 1998, 279, 208-211
- [55] Lee, S. T.; Zhang, Y. F.; Wang, N.; Tang, Y. H.; Bello, I.; Lee, C. S.; Chung, Y. W. Semiconductor nanowires from oxides. J. Mater. Res. **1999**. 14. 4503-4507
- [56] Shi, W. S.; Peng, H. Y.; Zheng, Y. F.; Wang, N.; Shang, N. G.; Pan, Z. W.; Lee, C. S.; Lee, S. T. Synthesis of large areas of highly oriented, very long silicon nanowires. Adv. Mater. 2000, 12, 1343-1345.
- Shi, W. S.; Peng, H. Y.; Wang, N.; Li, C. P.; Xu, L.; Lee, C. S.; Kalish, R.; Lee, S. T. Free-standing single crystal silicon nanoribbons. J. Am. Chem. Soc. 2001, 123, 11095-11096.
- [58] Lide, D. R. Handbook of Chemistry and Physics; 84th ed. Florida: CRC Press, 2003.
- [59] Deringer, V. L.; Dronskowski, R. Stability of pristine and defective SnTe surfaces from first principles. ChemPhysChem. 2013, 14,
- [60] Sugai, S.; Murase, K.; Katayama, S.; Takaoka, S.; Nishi, S.; Kawamura, H. Carrier density dependence of soft TO-phonon in SnTe by Raman scattering. Solid State Commun. 1977, 24, 407-409.
- [61] An, C. H.; Tang, K. B.; Hai, B.; Shen, G. Z.; Wang, C. R.; Qian, Y. T. Solution-phase synthesis of monodispersed SnTe nanocrystallites at room temperature. Inorg. Chem. Commun. 2003, 6, 181-184.
- Acharya, S.; Pandey, J.; Soni, A. Soft phonon modes driven reduced thermal conductivity in self-compensated Sn_{1.03}Te with Mn doping.

- Appl. Phys. Lett. 2016, 109, 133904.
- [63] Berchenko, N.; Vitchev, R.; Trzyna, M.; Wojnarowska-Nowak, R.; Szczerbakow, A.; Badyla, A.; Cebulski, J.; Story, T. Surface oxidation of SnTe topological crystalline insulator. Appl. Surf. Sci. 2018, 452, 134-140.
- [64] Neudachina, V. S.; Shatalova, T. B.; Shtanov, V. I.; Yashina, L. V.; Zyubina, T. S.; Tamm, M. E.; Kobeleva, S. P. XPS study of SnTe(100) oxidation by molecular oxygen. Surf. Sci. 2005, 584, 77-82.
- Mandale, A. B.; Badrinarayanan, S. X-ray photoelectron spectroscopic studies of the semimagnetic semiconductor system Pb_{1-x}Mn_xTe. J. Electron Spectrosc. Relat. Phenomena 1990, 53, 87-95.
- [66] Kobayashi, K. L.; Kato, Y.; Katayama, Y.; Komatsubara, K. F. Carrier-concentration-dependent phase transition in SnTe. Phys. Rev. Lett. 1976, 37, 772-774.
- [67] Brebrick, R. F. Deviations from stoichiometry and electrical properties in SnTe. J. Phys. Chem. Solids 1963, 24, 27-36.
- [68] Muldawer, L. New studies of the low temperature transformation in SnTe. J. Nonmetals. 1973, 1, 177-182.
- [69] Brillson, L. J.; Burstein, E.; Muldawer, L. Raman observation of the ferroelectric phase transition in SnTe. Phys. Rev. B 1974, 9, 1547-1551.
- Inoue, M.; Ishii, K.; Yagi, H. Ferromagnetic ordering in Mn-doped SnTe crystals. J. Phys. Soc. Japan 1977, 43, 903-906.
- Reja, S.; Fertig, H. A.; Brey, L.; Zhang, S. X. Surface magnetism in topological crystalline insulators. Phys. Rev. B 2017, 96, 201111.
- [72] Liu, J. W.; Fang, C.; Fu, L. Tunable Weyl fermions and Fermi arcs in magnetized topological crystalline insulators. Chin. Phys. B 2019, 28, 047301.
- [73] Chi, H.; Tan, G. J.; Kanatzidis, M. G.; Li, Q.; Uher, C. A low-temperature study of manganese-induced ferromagnetism and valence band convergence in tin telluride. Appl. Phys. Lett. 2016,
- [74] Inoue, M.; Tanabe, M.; Yagi, H.; Tatsukawa, T. Transport properties of SnTe-MnTe system: Anomalous Hall effect. J. Phys. Soc. Japan **1979**, 47, 1879–1886.
- Inoue, M.; Yagi, H.; Ishii, K.; Tatsukawa, T. Electrical resistivity of Mn-doped SnTe crystals at low temperature. J. Low Temp. Phys. 1976, 23. 785-790.
- [76] Taskin, A. A.; Yang, F.; Sasaki, S.; Segawa, K.; Ando, Y. Topological surface transport in epitaxial SnTe thin films grown on Bi₂Te₃. Phys. Rev. B 2014, 89, 121302
- [77] Siol, S.; Holder, A.; Ortiz, B. R.; Parilla, P. A.; Toberer, E.; Lany, S.; Zakutayev, A. Solubility limits in quaternary SnTe-based alloys. RSC Adv. 2017, 7, 24747-24753.
- [78] Van de Walle, C. G.; Neugebauer, J. First-principles calculations for defects and impurities: Applications to III-nitrides. J. Appl. Phys. **2004**. 95. 3851–3879.
- Wang, N.; West, D.; Liu, J. W.; Li, J.; Yan, Q. M.; Gu, B. L.; Zhang, S. B.; Duan, W. H. Microscopic origin of the p-type conductivity of the topological crystalline insulator SnTe and the effect of Pb alloying. Phys. Rev. B 2014, 89, 045142.